Nanoscale

PAPER

View Article Online
View Journal | View Issue

Cite this: *Nanoscale*, 2018, **10**, 22362

Switchable dissociation of excitons bound at strained CdTe/CdS interfaces†

Florian Enders, [a] Arne Budweg, [b] Peng Zeng, ‡[c] Jannika Lauth, §[d] Trevor A. Smith, [c] Daniele Brida [b,e] and Klaus Boldt *[a]

Received 30th September 2018,
Accepted 17th November 2018

DOI: 10.1039/c8nr07973k

rsc.li/nanoscale

Charge carrier dynamics of semiconductor nano-heterostructures are determined by band alignment and lattice mismatch of the adjacent materials. However, quantum efficiencies for the separation of excited charge carriers at such an interface are hard to predict and cannot yet be easily controlled. In this work we examine nanorods with a severely strained, axial CdTe/CdS interface using femtosecond transient absorption spectroscopy. We show that charge separation is mitigated by equal contributions of valence band distortion and formation of coulomb pairs across the interface. Left undisturbed such localised excitons relax rapidly *via* non-radiative recombination channels. By adding a competitive hole acceptor that disrupts the coulomb interaction we overcome the synergetic co-localisation of the carriers and realise charge separation. The thus created long-lived state can be exploited for a broad range of applications such as photocatalysis, water splitting, and switchable nanodevices.

Introduction

Colloidal semiconductor nano-heterostructures play a pivotal role in nanotechnology, because they combine size quantisation effects with features that arise from two different materials in electronic contact. They promise superior performance as fluorophores, in light harvesting, or as photocatalysts, while fine control over their physical properties can be exercised by means of chemical synthesis.[1–3] A further dimension of control is introduced *via* shape anisotropy. Nanorods and nanowires allow for effects to be directional in one dimension while preserving spatial confinement perpendicular to that axis. One of the most widely studied, anisotropic nano-heterostructures are CdS nanorods that have been grown from a CdSe seed.[4–8] In these particles excited holes localise in the potential well of the CdSe seed, while electrons can be either confined to the same volume or delocalised over the whole nanorod, depending on seed size and the thickness of the CdS shell. The transition from delocalised (*quasi* type-II regime) to localised electrons (type-I regime) occurs between CdSe seed sizes of 3 to 4 nm.[6,9,10] A similar system in which electrons and holes separate spatially at a heterointerface with staggered band alignment (type-II structure) has been fabricated using ZnSe nanocrystals as seeds in ZnSe/CdS nanorods.[5,11,12]

Different interpretations exist in the literature concerning the delocalisation and spatial separation of electrons and holes in these systems. Wu *et al.* have argued that a photoexcited electron remains close to the hole in CdSe/CdS nanorods. These appear as distinct bound states in femtosecond transient absorption (TA) spectra.[13] Transport of charge carrier pairs (excitons) along a 1D nanostructure on the typical length scales of these systems between 10 and 100 nm was found to be diffusion-limited.[14] Sánchez-Paradinas *et al.* have found reduced radiative recombination rates in extended aerogels, which were composed of the same nanorods connected at the tips. The longer lifetimes were interpreted as an increased degree of electron delocalisation beyond a single nanorod.[15] However, all reported lifetimes for CdSe/CdS support coulomb-bound excitons and holes localised in the potential well of the seed particles.[10]

Charge carrier dynamics are further complicated by surface states. It was shown that in pure CdS nanorods over 99% of the photoexcited holes get trapped in surface states within the first picoseconds after excitation, which is observed using TA spectroscopy as a weak, broad photoinduced absorption below

[a]*Department of Chemistry, University of Konstanz, 78457 Konstanz, Germany. E-mail: klaus.boldt@uni-konstanz.de*
[b]*Department of Physics, University of Konstanz, 78457 Konstanz, Germany*
[c]*ARC Centre of Excellence in Exciton Science, School of Chemistry, The University of Melbourne, Parkville, Victoria 3010, Australia*
[d]*Department of Chemical Engineering, Delft University of Technology, Van der Maasweg 9, NL-2629 HZ Delft, The Netherlands*
[e]*Faculty of Science, Technology and Communication, University of Luxembourg, 162 A, Avenue de la Faïencerie, L-1511 Luxembourg*

†Electronic supplementary information (ESI) available: Parameters used in EMA calculations, full 2D TA spectra, and additional kinetic data. See DOI: 10.1039/c8nr07973k

‡Present address: School of Materials and Energy & Center for Applied Chemistry, University of Electronic Science and Technology of China, Chengdu 611731, P.R. China.
§Present address: Institute for Chemistry, Carl von Ossietzky University, Carl-von-Ossietzky-Str. 9–11, 26129 Oldenburg.

the band gap.[14] In seeded rods this mechanism competes with localisation of holes in the potential well of the seed. Dukovic and co-workers have found that trapped holes conceal effects of different seed materials (CdSe, ZnSe, CdS) and thus band alignment on the electron dynamics, as de-trapping of holes becomes the rate-determining step for exciton recombination.[16,17] These dynamics become relevant in more complex systems, in which the carrier dynamics is driven by interaction between two or more recombination centres. Examples are charge separation in photovoltaics,[18] two half reactions with different kinetics in photocatalysis,[19] two-colour emission, mutual bleaching of the excitonic states, and fluorescence upconversion.[20,21] Many anisotropic systems with controlled band gap alignments have become available in recent years with which to study charge carrier dynamics, including nanorods with selective growth of semiconductors[20–23] or metals[24–27] on one or two tips. It is highly advantageous for applications of these systems to introduce a mechanism that controls the dynamics by external triggers.

A general issue for the fabrication of heterostructures is lattice mismatch between the crystalline phases in contact, which introduces hydrostatic strain on the crystal lattices. The full effects of strain on nanocrystals is not yet completely understood. Smith *et al.* have shown that compression of small nanocrystals by a mismatched shell distorts the electronic structure strongly enough to shift it between the type-I and type-II regime.[28] A deviation from the type-I behaviour of CdSe/CdS seeded nanorods with large (>4.5 nm) seeds was attributed to strain by Angeloni *et al.*[10] Christodoulou *et al.* have shown for much larger CdSe/CdS rod-in-rod nanocrystals that lattice mismatch between core and shell leads to piezoelectric potentials at the opposite ends of the elongated seed. These also cause band distortions that lead to formation of a type-II system.[29] The tendency of the structure to minimise strain leads to formation of crystal defects and, for higher strain, anisotropic rather than epitaxial growth.[30,31] Of the II–VI semiconductors CdTe has one of the highest compressibilities[28] and forms a strongly mismatched type-II interface with CdS, for which large strain effects can be expected.[32–34] While this material combination is employed widely for thin film solar cells[35,36] relatively few studies are concerned with the CdTe/CdS interface in colloidal nanocrystalline systems and focus on core/shell systems. The band gap alignment was tuned between type-I for strongly confined systems and type-II for larger cores and thicker shells.[37–39] Characteristically long fluorescence lifetimes >200 ns and loss of definition of the excitonic features in the absorption spectrum were reported by Schöps *et al.* and Watanabe *et al.*, which was attributed to the reduced wave function overlap of the type-II state.[32,40] The decay time and Stokes shift were found to increase with temperature above 120 K, due to a thermal activation from a localised interface state to the lower-lying charge-separated state. Furthermore, trap states at the interface and the surface of the heterostructures were shown to have a significant influence on the relaxation dynamics. Trap-induced absorption from both electrons and holes were reported in the range of 600–750 nm with an intensity that depends on the shell thickness.[41] The influence of these traps is expected to be even more relevant when investigating heterointerfaces that deviate from the core–shell geometry where both electron and hole are subjected to a variety of different trap states.

In our study we demonstrate using ultrafast TA spectroscopy and effective mass calculations that after photoexcitation of CdSe/CdS nanorods carrying a CdTe tip (CdTe@CdSe/CdS) both electrons and holes localise close to the strained CdTe/CdS interface. Charge localisation is facilitated by a combination of strain-induced band distortion and coulomb interaction. While this state can rapidly depopulate by non-radiative processes we were able to recover the electron *via* a competitive channel in which the hole is actively extracted through the addition of a hole acceptor. Furthermore we show how the thickness of the nanorod influences the charge carrier relaxation behaviour in the system due to quantum confinement effects, with charge separation being more hindered in thinner nanorods. These results illustrate that while lattice mismatch can dominate the electronic structure of semiconductor heterojunctions the strained interface introduces a means to switch charge separation on and off by a chemical stimulus.

Experimental section

Chemicals

CdO (>99.5%), oleic acid (>99%), tri-*n*-octylphosphine (TOP, 97%), tri-*n*-octylphosphine oxide (TOPO, 99%), *n*-hexylphosphonic acid (HPA, 95%), 1-octadecene (ODE, 90%), and methanol were purchased from Sigma-Aldrich. *n*-Octadecylphosphonic acid (ODPA, >99%) was purchased from PCI Synthesis. Chloroform (99.9%) and oleylamine (>80–90% C_{18}) was acquired from Acros. Selenium shot (99.999%) was purchased from Alfa Aesar, 4-mercaptophenol (4-MPH, 95%) and tellurium shot (99.9999%) were purchased from ABCR, toluene (>99.5%) from Carl Roth, and acetone (>99%) from VWR. All chemicals were used as is without further purification.

Particle synthesis

CdSe seeds and CdSe/CdS seeded rods were prepared following the protocol reported by Carbone *et al.*[42] CdTe tip growth was adapted and optimised from a seeded growth protocol for CdSe tips on CdS nanorods originally published by Deutsch *et al.*[21] A three-neck flask equipped with a condenser, thermocouple and septum was loaded with 1.44 g TOPO, 1.6 mL ODE and 1.6 mL oleylamine and the mixture was degassed under reduced pressure at 80 °C for 1 h. The flask was then flooded with nitrogen and 0.8 mL (16 nmol) of a dispersion of CdSe/CdS seeded nanorods in TOP were added under inert gas conditions. The reaction mixture was heated to 200 °C and 0.48 mL of Te in TOP (0.1 M) were added with a syringe pump over 1 h. This was followed by the addition of 0.24 mL of Cd oleate in ODE (0.1 M) over 30 min. The colour of the solution turned from bright orange to green/brown, depending on the

size of the initial rods. After the addition was complete, the particles were annealed for 10 min at 200 °C. The reaction mixture was then cooled to 80 °C and 5 mL dry $CHCl_3$ were added. The particles were transferred into a centrifuge vial under inert gas conditions and flocculated using a 2.5-fold excess of dry acetone, centrifuged, and redispersed in dry $CHCl_3$. This purification procedure was repeated twice. The resultant dispersion was passed through a 200 mesh PTFE syringe filter and stored in a glove box.

Characterisation

Steady-state UV/vis absorption spectra were acquired using an Agilent Cary 60 spectrometer. PL spectra were obtained from a PicoQuant FluoTime-300 spectrophotometer. All PL quantum yields were measured using an excitation wavelength of 480 nm. High-resolution TEM micrographs were obtained using a Jeol JEM 2200FS transmission electron microscope operated at 200 kV. Samples were prepared by drop-casting 10 μL of dilute sample solution in toluene onto a carbon-coated copper grid (Quantifoil).

Femtosecond transient absorption measurements

TA spectroscopy was performed on diluted samples in fused silica absorption cells with an optical path length of 2 mm using three different setups: to access a broad spectral range (450–750 nm) an instrument using a high repetition rate Ti:sapphire regenerative amplifier system (Coherent RegA 9050, 92 kHz, centred at 800 nm) as the laser source was employed (P.Z. and T.A.S.). The output was re-compressed (Coherent EC9150) to ~60 fs before being split to generate pump and probe pulses. A portion of the 800 nm amplifier output was used to generate the pump beam using an optical parametric amplifier (OPA, Coherent 9450). The visible broadband probe with a range of approximately 440–760 nm (1.63–2.82 eV) was generated from the residual fundamental 800 nm (1.55 eV) beam focused onto a 3 mm sapphire crystal (Crystal Systems). A notch filter was used to block the fundamental pulse in the probe beam. Pump and probe pulses were weakly focused and overlapped at the sample with an off-axis parabolic mirror with pump spot size of 200 μm in diameter. The pump beam was mechanically chopped at and synchronised to a twentieth of the amplifier pulse repetition rate (4.6 kHz). The delay between pump and probe pulses was controlled using a motorised delay stage (Newport UTM-PP0.1, with step size of 0.66 fs and range of 800 ps). After passing through the sample, the probe beam was analysed with a CMOS detector (Ultrafast Systems) at 9200 spectra per second. The pump beam had an excitation density of <200 μJ cm^{-2} per pulse (<10^{14} photons per cm^2) in order to eliminate multiexciton effects and was polarised 54.7° with respect to the probe.

To access wavelengths greater than 700 nm a HELIOS spectrometer (Ultrafast Systems) was used (J.L.). Samples were studied using a broadband pump–probe set-up described previously and briefly discussed here.[43] Femtosecond laser pulses (~180 fs) were generated in a Yb:KGW oscillator at 1028 nm and amplified (Light Conversion, Pharos SP). The 1028 nm fundamental beam was split into a pump and probe beam. The pump beam energy was varied by nonlinear frequency mixing inside an OPA. A broadband probe spectrum (500–1500 nm) was generated by focusing a small portion of the fundamental laser light onto a sapphire crystal. The delay of the probe pulse was realised by an automated delay stage. Samples were photoexcited with energy densities of ~10–100 μJ cm^{-2}. The pump pulses were dumped after photoexcitation of the sample, while the probe light was led to a detector fibre suitable for the probe spectrum selected (HELIOS, Ultrafast Systems).

High temporal resolution was achieved using a spectrometer with a Yb:KGW regenerative amplifier system (Light Conversion, Pharos) operating at a repetition rate of 50 kHz (A. B. and D.B.). A home-built noncollinear optical parametric amplifier (NOPA) delivered narrow band pump pulses either at a central energy of 542 nm (2.289 eV) with a bandwidth of 36 meV or at a central energy of 640 nm (1.937 eV) with a bandwidth of 30 meV. In both cases the pulses were compressed to a duration of approximately 50 fs by means of dielectric chirped mirrors. In the spectral range between 506 and 800 nm (1.55–2.45 eV) the induced transmission change was probed with light from a super continuum generated in a 2 mm thick sapphire crystal. The pulses were compressed using custom made dielectric chirped mirrors. In addition, the differential transmission signal at 460 nm (2.7 eV) was probed with the second harmonic of another home built NOPA. A curved mirror with a focal length of f = 30 cm deflected both pump and probe beam to a common spot where they overlapped with a small angle to separate the beams after sample interaction. With a focal size of 100 μm for pump and 70 μm for the probe beam an excitation density of 200 μJ cm^{-2} was reached. After sample interaction the probe pulses were spectrally dispersed using a 0.15 m long spectrograph with a 300 g mm^{-1} grating and individually detected by a high speed CCD chip at the repetition rate of the laser system.[44] In combination with a modulation of the excitation pulse train at half the repetition rate, spectra of subsequent probe pulses were used to calculate the differential transmission signal.

Samples were prepared in a nitrogen glove box with a constant concentration of particles per total volume for each batch of particles. The cuvettes were sealed with a PTFE stopper and dipped into molten paraffin to protect the samples from air and moisture. All spectra were corrected for the chirp of the supercontinuum probe.

Results and discussion

We synthesised CdTe@CdSe/CdS tipped nanorods using a seeded growth approach starting from CdSe/CdS seeded rods.[42] Two seed diameters, 2.9 and 4.0 nm, were employed to account for *quasi* type-II and type-I behaviour, with rod lengths of 30.4 ± 2.5 and 36.5 ± 3.8 nm, respectively. CdTe tips were grown by adapting the protocol for tip-selective growth of CdSe published by Oron and co-workers.[21] UV/vis absorption and PL

spectra, as well as TEM micrographs before and after tip growth are shown in Fig. 1 for the sample made from 2.9 nm CdSe seeds and 30 nm long CdS rods.

The size of the CdTe tips varies between 5 and 10 nm and is controlled by the concentration of the initial CdSe/CdS nanorod dispersion relative to the added Te and Cd precursors. High-resolution TEM micrographs show that the CdTe tips form only on one side of the rods and attach with their {111} facets to the $\{10\bar{1}\bar{1}\}$ facets of CdS, with an angle of 31.4° with respect to the CdS *c*-axis (see ESI, Fig. S1†). This polar facet forms when the faster growing, high energy $(000\bar{1})$ end of the nanorods is eliminated.[24,45,46] We explain selective CdTe growth by the lack of inversion symmetry of the wurtzite crystal structure, leading to chemically different facets, combined with the 11.5% lattice mismatch between CdS and CdTe.[47] Compared to nucleation of new seeds on CdS, growth of already formed tips is therefore strongly favoured under thermodynamic control, which was guaranteed by slow precursor addition at high temperatures. The same mechanism leads to a position of the CdSe seed at 2/3 to 3/4 of the length of the nanorods,[9,42] which results in a defined spatial separation between seed and CdTe/CdS interface.

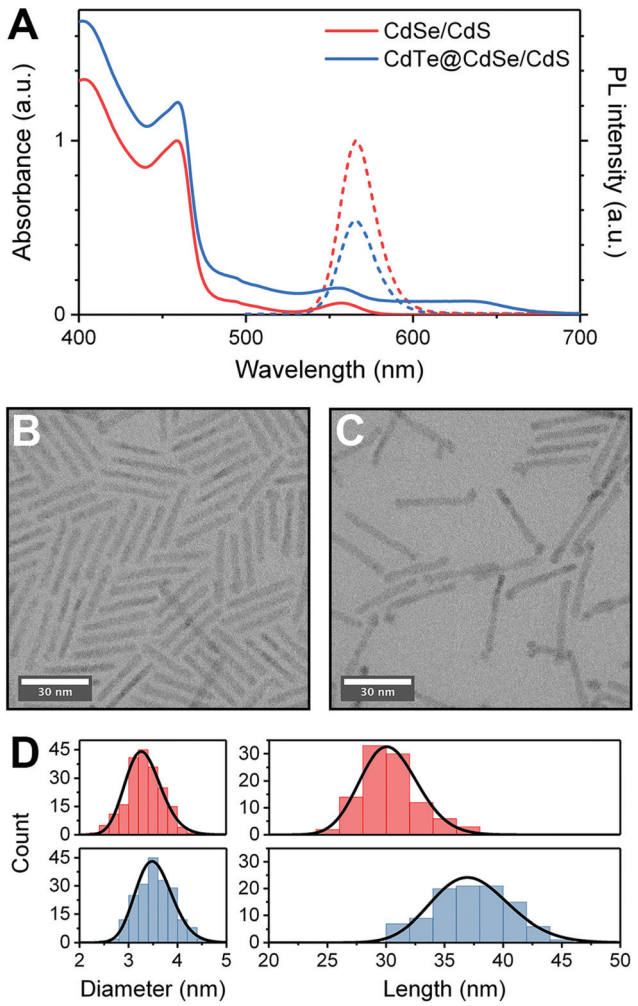

Fig. 1 (A) UV/vis absorption (solid lines) and PL spectra (dashed lines) of CdSe/CdS nanorods (red) and CdTe@CdSe/CdS tipped nanorods (blue). Absorption spectra are normalised to the CdS absorption edge of tipless CdSe/CdS nanorods and reflect the increased signal due to the CdTe tip. The PL spectra were excited with light at the wavelength of 350 nm and are normalised relative to their PL QY. Shown below are TEM micrographs of CdSe/CdS (B) and CdTe@CdSe/CdS (C) and histograms of the size distribution for CdSe/CdS (top, red) and CdTe@CdSe/CdS (bottom, blue).

We first look at the CdSe/CdS seeded nanorods with smaller 2.9 nm seeds. These exhibit a strong absorption edge at 468 nm, corresponding to the CdS band edge state. Weaker absorption maxima at 557 and 494 nm result from excitonic states in the *quasi* type-II structure of the CdSe seed embedded in CdS. The seeded rods strongly fluoresce at 567 ± 22 nm. After growth of the CdTe tip the sample colour changes from bright orange to brown and an additional broad, featureless absorption down to 658 nm with an optical density comparable to that of the CdSe absorption can be observed. This signal can be explained well by inhomogeneous broadening from the size distribution of the CdTe tips and the formation of a spatially indirect type-II state: small wave function overlap between electron and hole leads to low oscillator strength and an expected lack of defined, excitonic peaks.[2] The photoluminescence quantum yield (PL QY) drops from 42% to 17% after CdTe growth, but the shape of the PL spectra does not change. Averaged fluorescence lifetimes are 24.7 and 14.1 ns for the samples without and with CdTe tip, respectively (see ESI, Fig. S2†). We therefore attribute the PL to direct excitation of the CdSe transitions, while excitation of the CdTe/CdS interface does not lead to any fluorescence.

Electronic structure calculations

We calculated the band structure of the CdTe@CdSe/CdS nanorods using the 3D effective mass approximation (EMA) provided by the software package next**nano**++.[48] A geometric model of the nanorod with hexagonal cross section was used (see ESI†) and all material constants have been taken from Adachi *et al.*,[49] except for valence band offsets, for which calculated values by Wei and Zunger have been used (see ESI, Table S1†).[50] The calculations included minimisation of hydrostatic strain, but did not account for coulomb interaction between charge carriers. EMA as a continuum method neglects the atomistic nature of the semiconductor that becomes important at small sizes, as well as multi-band coupling.[51] It is therefore limited in its absolute predictive power; however, it allows to efficiently calculate large nanocrystals and allows trends to be identified for charge carriers close to the Γ point of the 1st Brillouin zone. Fig. 2 depicts the band edges for the conduction band and for the heavy hole (hh), light hole (lh) and spin–orbit split-off hole (so) valence bands, as well as the lowest energy levels and wave functions for both electron and hole, along the *c*-axis at the center of the nanorod (for calculations with 4.0 nm CdSe seeds see ESI, Fig. S3†).

The calculations predict that the wave function of an electron in the conduction band will be centred at the site of the lowest potential energy, which is the CdSe seed, but spread

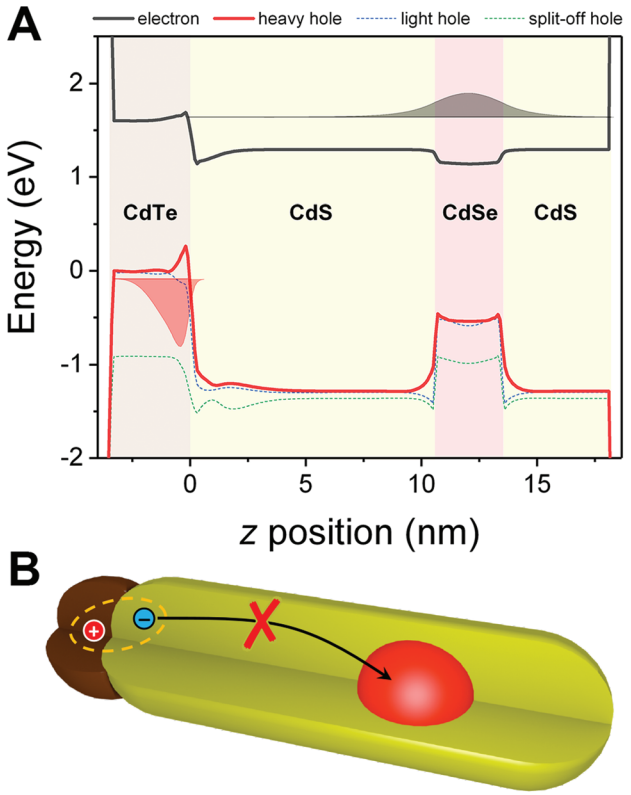

Fig. 2 (A) Calculated band structure of a CdTe@CdSe/CdS tipped nanorod with a 2.9 nm CdSe seed, and hexagonal cross section along the wurtzite [0001] axis. Band edges of the conduction band and three valence bands are shown, as well as the lowest energy level and wave function for electron (black) and hole (red). (B) Cartoon depiction of the structure showing the inhibited electron transfer from the CdTe/CdS interface to the CdSe seed.

into the surrounding CdS shell. The CdTe/CdS interface acts as a potential barrier for the first quantised state of the electron and none of the first 4 electron wave functions have significant amplitude in the CdTe tip (see ESI, Fig. S4†). In the valence band two potential wells are found at the location of the CdSe and CdTe particles. The two minima are separated by the potential barrier of the CdS rod, which is high enough to suppress the flow of charges between the minima. The CdSe/CdS interface is only weakly strained and the calculations reproduce earlier *ab initio* studies by Luo *et al.*[7] However, the valence band (hh) is strongly distorted at the CdTe/CdS interface. The depth of the strain-induced potential trough increases with larger contact area (see ESI, Fig. S5†) and leads to localisation of the lowest energy hole state close to the interface. Increasing the volume of the CdTe tip partially delocalises the hole, but does not significantly shift the maximum of the lowest energy wave function (see ESI, Fig. S6†). Spatial confinement of the band-edge hole is thus considerably stronger than what would be expected from the size of the CdTe tip alone. The conduction band at the interface is less strongly distorted on the CdS side of the interface and localisation of the electron is not affected.

Coulomb-mediated exciton localisation

The calculations demonstrate that strain effects are expected to strongly affect the carrier localisation and dynamics at the CdTe/CdS interface, but give no information on charge carrier interactions. We therefore performed TA spectroscopy on the nanorod samples, in which we selectively excited the CdTe/CdS interface (≥620 nm) or both recombination centres (540 or 560 nm). The excitation energy was held below the CdS absorption edge, and the photon flux was kept below 200 μJ cm^{-2} to avoid excitation of biexcitons. The complete TA data can be found in the ESI, Fig. S7–S20.†

First we obtained spectra of the CdSe/CdS seeded rods that were used to grow the CdTe tips, exciting the sample with light pulses with a central wavelength of 560 nm and a bandwidth of 2.6 nm (see Fig. 3A). In accordance with previous reports in the literature a bleaching signal from the band edge exciton

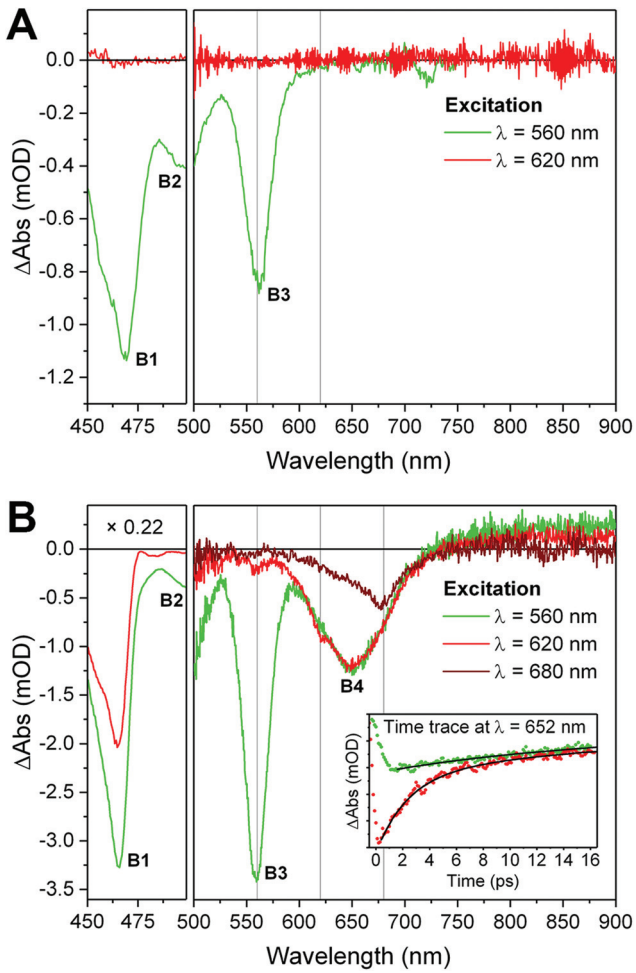

Fig. 3 TA spectrum of (A) CdSe/CdS nanorods and (B) CdTe@CdSe/CdS tipped nanorods 1 ps after excitation with light pulses at central wavelengths of 560 (green), 620 (red), and 680 nm (brown) and a pump fluence of ~100 μJ cm^{-2}. A factor of 0.22 was used to scale the spectral range between 450 and 500 nm for the tipped rods. The inset shows the decays of B4 after excitation with 560 (green) and 620 nm (red) light, with a fits to a biexponential function in black.

(B3, $1S_e$–$1S_{3/2}$) at 555 nm was observed, along with bleaching at higher energy (B2, $1S_e$–$2S_{3/2}$ at 498 nm and B1, $1S_e$–$1S_{CdS}$ at 468 nm) that are caused by state filling of the $1S_e$ electron. The strong signal at 468 nm corresponds to a state of the CdS rod and is only observed for seed sizes below ~3.8 nm, in which the electron wave function delocalises into the CdS shell in a *quasi* type-II configuration.[9] All bleaching signals appear constant on the timescale of the TA experiment, which is in accordance with the PL lifetime >10 ns. With an excitation wavelength of 620 nm, below the band gap of the structure, no signals are observable.

The CdTe-tipped nanorods show the same signals with no spectral shift when excited with light pulses with a central wavelength of 560 nm. In addition, a bleaching signal B4 at 650 nm is observed that is 2.4 times broader than the CdSe band edge bleach and corresponds to excitation of either the CdTe tip or the CdTe/CdS interface (see Fig. 3B). The ΔAbs of the CdS-related B1 is increased 7-fold compared to rods without a tip. Above 750 nm a weak, broad photo-induced absorption can be seen, which has been attributed to holes trapped on the CdS surface.[14,17,52] When shifting the pump wavelength to 620 nm (3.4 nm bandwidth), below the band gap of CdSe, the signals B2 and B3 are not observed. However, B1 is still present with 60% of the signal strength after 1 ps. The remaining signal is in very good agreement with the drop of PL QY from 42% to 17% after tip growth (60% decrease), as well as the ratio between the integrals of B3 and B4 when exciting both recombination centres at 560 nm. Here, B4 makes up 47% of the total signal. This reflects the distribution of light absorption over the two possible band gap states according to their respective absorption coefficients. Both the CdSe seed and the CdTe/CdS interface show bleaching in the spectral region of B1, but are sufficiently decoupled to not influence each other by state filling. Relative errors can be attributed to the differences in oscillator strength of the excitonic states and partial overlap of B1 and B2.

B4 is a pronounced peak, compared to the broad, featureless signal observed in the steady state absorption spectrum in Fig. 1A. When using even lower pump energies (1.82 eV, 680 nm) only the most strongly red-shifted fraction of the particle ensemble is excited, which leads to a narrowed signal and points to a well-defined interface state that is heterogeneously broadened. Further evidence for a confined, interfacial state comes from the photo-induced absorption at wavelengths >750 nm, which becomes smaller as the pump photon energy is lowered and is no longer visible when pumped at a wavelength of 680 nm (3.8 nm bandwidth). It implies that trapping of the hole by a broad distribution of surface states occurs only from exciting the CdSe seed and from hot holes, but not from the CdTe/CdS ground state.[9]

We performed a global fit of the TA spectra using a parallel decay model of the Glotaran software package.[53] The temporal resolution was determined by fitting the rise time with a Gaussian function, which yielded a width of 50 fs in the spectral range of 520–720 nm and 120 fs at 460 nm. As can be expected when directly exciting a band edge exciton all bleaching signals appear within the temporal resolution, except for B4 when exciting at 540 nm. Here the rise time increases towards longer wavelengths of the probe pulse from <100 fs at 620 nm to 340 fs at 660 nm. This delay is consistent with hot carrier relaxation for both holes and electrons with spatially coupled holes, as shown by Cooney *et al.*[54] Close inspection of B4 reveals an ultrafast decay component with a time constant of 170 fs, which we attribute to electron cooling from CdTe into the CdTe/CdS interfacial state. Both states have similar transition energies and the decrease of signal is caused by the concomitant drop in oscillator strength. This ultrafast component can be seen in the inset to Fig. 3B.

Table 1 summarises the decay kinetics. We consistently found two decay constants for the bleaches B1 and B4, independent of excitation wavelength: a very rapid decay with $\tau_1 \approx 2$ ps was found in all samples, while the second decay scaled inversely with the rod thickness, yielding $\tau_2 \approx 73$ ps for thin and $\tau_2 \approx 15$ ps for thick nanorods. In contrast, B3 is a long-lived state and remained constant on the timescale of the experiment. When exciting below the CdSe band gap at a wavelength of 640 nm B3 was very weak for the thin rods. For the thicker rods the buildup time $\tau_{B3} = 15$ ps matches the decay of B4. This suggests transfer of the electron from the CdTe/CdS interface to the CdSe seed with a ~13% quantum yield, as direct excitation of B3 could be excluded from the lack of any signal when pumping CdSe/CdS nanorods without tips.

From these data we derive a two-factor model for charge localisation at the CdTe/CdS interface: strain-induced band bending confined the hole close to the interface in the CdTe tip. The distortion of the conduction band is not large enough to confine the electron in a similar manner. However, the additional coulomb potential of the hole is sufficient to quantitatively trap the electron at the interface as well. The depth of the coulomb potential well can be approximated using the average static dielectric constant $\bar{\varepsilon} \approx 9.46$ between electron and hole and is in the order of a few 100 meV for distances $R_{eh} < 1$ nm.

$$E_{coulomb} = -\frac{e^2}{4\pi\bar{\varepsilon}\varepsilon_0 R_{eh}}.$$

This is in good agreement with previous reports, which give coulomb interaction in a range between 75 and 400 meV, with

Table 1 Lifetime components of the bleaches B1, B3, and B4 for two CdSe seed diameters and excitation wavelengths of 540 and 640 nm

		D_{CdSe} = 2.9 nm		D_{CdSe} = 4.0 nm	
Signal	λ_{ex} (nm)	τ_1 (ps)	τ_2 (ps)	τ_1 (ps)	τ_2 (ps)
B4	540	2.1	—	1.9	—
	640	1.7	73.4	1.8	17.5
B3	540	$(\infty)^a$	—	$(\infty)^a$	—
	640	-20.9^b	—	-14.8^b	—
B1	540	1.2	71.8	2.1	14.8
	640	2.5	73.5	1.7	12.1

[a] The signal is constant on the timescale of the experiment. [b] Negative lifetime indicates increasing signal.

150 meV for excitons in CdS nanorods with a 1.6 nm Bohr radius.[13,55,56] The value is in the same order of magnitude as the strain-induced band deformation of the conduction band, as indicated in Fig. 2A. The combination of these effects enables binding of the electron close to the interface. The quantum confined states of the undistorted CdS block carrier transport to the CdSe seed. This occurs quantitatively in case of the thin rods, while some electrons are able to overcome the lower barrier of the thicker rods. The majority of excitons recombines quickly and non-radiatively *via* coulomb-mediated electron–phonon coupling.

Hole acceptor-induced charge separation

The observations demonstrate that lattice mismatch at a heterointerface dominates carrier dynamics and may quantitatively suppress exciton dissociation in the type-II structure. However, due to the approximately equal contributions band bending and coulomb attraction it should be possible to delocalise the electron from the interface and recover the state responsible for the signal B3 by fast extraction of the hole from the nanostructure. The electron can thus be made available for a potential application, for example to catalyse a reduction reaction or in photovoltaics. Here we employed 4-mercaptophenol (4-MPH) as a hole scavenger, which has been shown to be capable of extracting holes from CdTe.[57]

To verify our hypothesis we added a 500-fold excess of 4-MPH to the CdTe@CdSe/CdS nanorods and excited the sample with laser pulses with a central wavelength of 640 nm and a bandwidth of 10 nm. The recovery of B3 was observed for all samples, at 560 nm for the sample using thin rods and at (see Fig. 4) and at 590 nm for thick ones (see Fig. 5). To quantify the increase of the signal we subtracted the time trace acquired in the absence of 4-MPH under otherwise identical conditions. The remaining signal is proportional to the fraction of electrons that have migrated to the CdSe seed as a result of hole transfer. In the case of thin nanorods it accounts for 70% of the total ΔAbs at 560 nm and grows with a time constant of τ_{B3} = 7.1 ps and τ_{B1} = 7.2 ps. The transfer is also reflected in a faster decay of B4, which decays biexponentially with τ_1 = 1.4 ps and τ_2 = 49.6 ps. This explains the relatively small recovered signal of B3, because the hole transfer can only compete with τ_2 and not with the much faster decay characterised by τ_1. The reduction of the lifetime τ_2 by 1/3 suggests that 33% of the particles in which the fast decay is absent undergoes successful hole transfer and electron relocalisation.

For thick nanorods the acceptor-induced growth has a time constant τ_{B3} = 4.8 ps, 1.5 times faster than for thinner rods, due to the reduced quantum confinement. In addition, the transition from *quasi* type-II to type-I band alignment of the CdSe/CdS region causes a much stronger confinement of the electron in its final state. The thicker rods were found to be slightly tapered with a thicker end at the position of the seed and a thinner one at the site of the tip. This shape may further act as a funnel for the electron towards the CdSe seed.

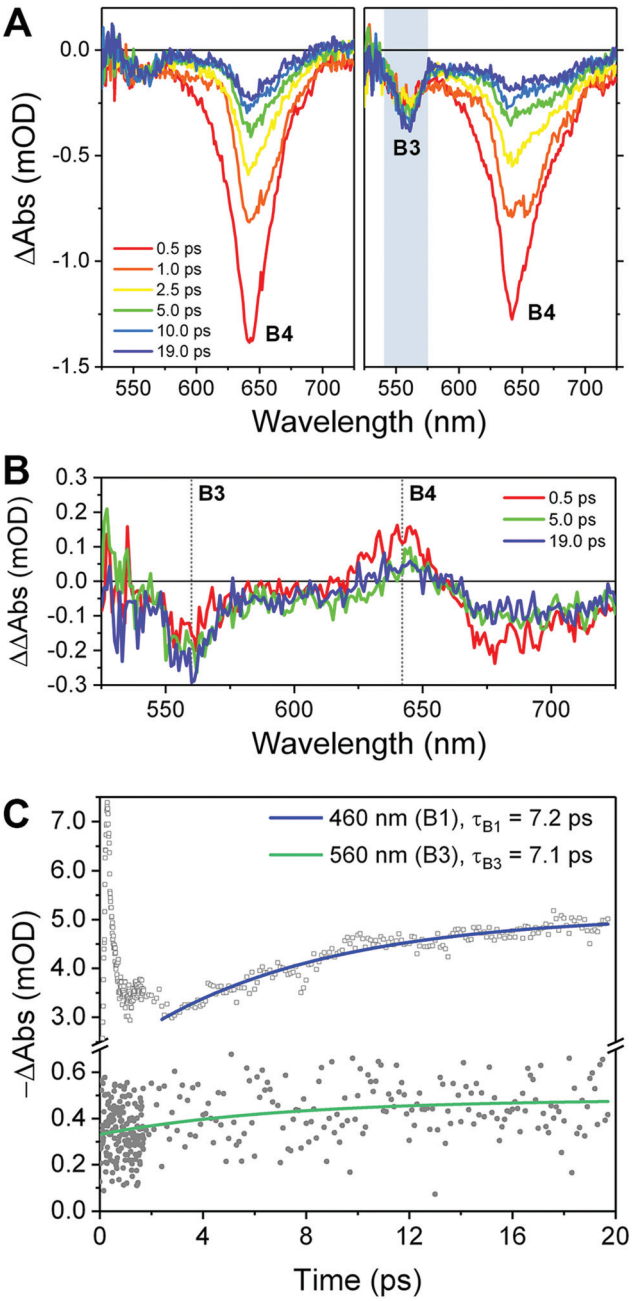

Fig. 4 (A) Series of TA spectra of CdTe@CdSe/CdS nanorods with 2.9 nm seeds excited at a wavelength of 640 nm without (left) and with (right) 500-fold excess of 4-mercaptophenol. (B) Difference spectra ΔΔAbs = ΔAbs_{4MPA} − ΔAbs between experiments in the presence and absence of the hole scavenger reveal the transfer of electrons from B4 to B3. (C) Difference of the time traces for the spectra above at λ = 460 nm (blue) and 560 nm (green) showing the grow-in of the B1 and B3 bleaches. The sharp peak in the blue trace below 1 ps is a result from the coherence artefact.

Charge carrier dynamics

When the hole is scavenged by 4-MPH the energy ΔE_{ht} gained from the transfer must compensate the coulomb energy $E_{coulomb}$ that binds the exciton at the CdTe/CdS interface. Any

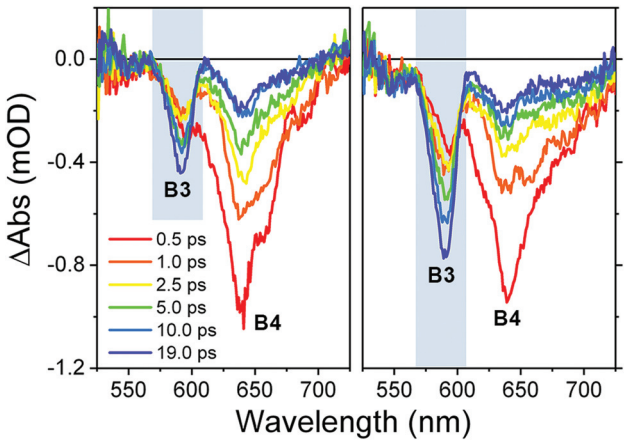

Fig. 5 Series of TA spectra of CdTe@CdSe/CdS nanorods with 4.0 nm seeds excited at a wavelength centred around 640 nm without (left) and with (right) 500-fold excess of 4-mercaptophenol.

excess energy $E_{Auger} = \Delta E_{ht} - E_{coulomb}$ may be used to lift the electron out of its shallow potential well and delocalise it into the $1S_e$ state of the CdS nanorod. The rate of this process will scale with the number of adsorbed quencher molecules that overlap with the hole wave function,[58] and depend on whether ΔE_{ht} suffices to release the electron. The electron re-localisation therefore utilises the large lattice mismatch between the two materials to form a switchable nanomaterial: a long-lived, excited electron is created in the presence of a sacrificial hole acceptor, while the exciton is deactivated quickly before the charges can be put to use in the unperturbed state. The competing, non-radiative pathways are characterised by the two time constants $\tau_1 \approx 2$ ps and $\tau_2 < 100$ ps. The fast component must be regarded as a detrimental process, because it dissipates a large fraction of the excitation energy before it can be used in any application. As we show in the following paragraphs this limitation can be overcome, because the strain-induced band-bending and the fast relaxation are not caused by the same structural property.

Fast relaxation in nanocrystals is commonly attributed to localised trap states. Two kinds of traps can be expected in our system: defects at the strained interface and surface states on CdTe. Point defects (D) reduce the large strain of the mismatched lattices. These give rise to a self-trapping mechanism for the exciton in which the charges form a D^+–D^- pair by first trapping one carrier at the defect, followed by localisation of the other one close by to compensate the charge. The resulting dipole distorts the lattice and allows for strong exciton–phonon coupling that is able to dissipate the excitation energy non-radiatively at much faster rates than that of exciton recombination.[59] Spatial confinement of the exciton at the strained interface strongly increases the probability for this relaxation pathway. This mechanism is a consequence of the mismatched lattice, the same effect that explains exciton localisation. Trap states on the particle surface are in principle independent of lattice distortions. A high density of surface traps near the valence band edge of CdTe nanocrystals has been identified by Boehme and co-workers.[60] These are based on Te–Te dimers to compensate incomplete coordination and facilitate electron trapping *via* an Auger-mediated process that dominates the decay of the band edge bleaching signal. Such an Auger process is unidirectional in favour of electron trapping, because of the much higher density of states in the valence band compared to the conduction band. Auger excitation of the electron by trapping a hole is blocked, because the energy released by the trapping process is much smaller than the separation of electron energy levels.[61] Spatial confinement of the hole at the interface is expected to further enhance Auger-mediated trapping, because it broadens the momentum spectrum of the wave function in Fourier space and relaxes requirements for momentum conservation.[62] At the same time the overlap between CdTe surface traps and the electron wave function localised at the CdS side of the interface is expected to depend on the area of the interface rather than the CdTe tip size.

Surface oxidation could be excluded as a source of trap states by looking at the TA spectra in the presence of air or water. We transferred two aliquots of CdTe@CdSe/CdS with 2.9 nm seeds into water by employing a ligand exchange against thioglycolic acid.[15] One of the samples was produced using deaerated solvents, while air-saturated water was used for the second sample. The deaerated sample exhibits the same behaviour as the one in chloroform. However, contact with oxygen causes a strong photoinduced absorption signal that extends from the position of B3 beyond our spectral window at 790 nm, with a rise time $\tau_{PA,rise} = 1.5$ ps and a decay time $\tau_{PA,decay} = 3.7$ ps (see ESI, Fig. S10 and S11†). An oxidised surface is therefore optically active and would be clearly observed in the TA spectra.

Suppression of surface traps

To identify the source of the fast decay component we performed a control experiment to compare the decay times of B4 that of spherical CdTe nanocrystals with a band edge absorption at $\lambda = 655$ nm ($D = 4.5$ nm). These spectra were acquired with the same pump pulse centred at 640 nm. Both systems yielded lifetimes of the same order of magnitude: $\tau_1 = 2.6$ ps and $\tau_2 = 41.4$ ps for CdTe compared to $\tau_1 = 1.7$ ps and $\tau_2 = 73.8$ ps for CdTe@CdSe/CdS (see Table 1). Kirkwood *et al.* have shown that surface traps on CdTe can be passivated by treating the particles with $CdCl_2$ in oleylamine for 15 minutes at 95 °C. Using this treatment they were able to passivate anionic trap states and increase PL QY from below the detection limit up to 80%.[63] In our experiments the PL QY of the CdTe nanocrystals increased from 8 to 50%. The corresponding band edge bleaching signal in the TA spectrum was fit by a single exponential decay with a lifetime of 780 ps, longer than the temporal window of the experiment. The PL QY of $CdCl_2$-treated, tipped nanorods increased by a factor of 2 and a broad peak centred at 725 nm appeared. Its average PL lifetime $\langle\tau_{PL,\ 713\ nm}\rangle = 213 \pm 12$ ns could be fitted with either a triple exponential or a stretched exponential function to account for inhomogeneous broadening. It is very long compared to $\langle\tau_{PL,\ CdSe}\rangle = 9.3 \pm 0.8$ ns for the CdSe seed emission and can be

attributed to either emission from the type-II exciton at the CdTe/CdS interface or to trap emission. The intensity of the broad signal was strongly reduced if dry solvents were used for purification, and the signal overlaps with the photoinduced absorption of surface-oxidised nanorods discussed in the previous section (see ESI, Fig. S11†). The Stokes shift of 230 meV is large compared to the shift of 100 eV reported for CdTe/CdS core/shell particles.[40] The PL excitation spectrum obtained from the broad emission shows signals corresponding to CdTe and CdS, but not CdSe, linking the emission to the CdTe/CdS interface (see Fig. 6B). The most convincing explanation for the PL is thus emission involving surface traps, likely due to $Cd(OH)_2$ from the reaction of $CdCl_2$ with moisture. This result is surprising, because no trap emission was found for the pure CdTe particles, and thus requires a trapping process that is directly linked to the presence of CdS or the CdTe/CdS interface. Interestingly, the PL decay at 565 nm (CdSe seed) had a long tail up to 3 μs with ~1% of the total intensity. It could be fitted with a $t^{-1.67}$ power law (see inset of Fig. 6A). Power law behaviour with a matching exponent has been observed for off-time distributions in quantum dot fluorescence blinking.[64,65] Dukovic and co-workers report similar behaviour for CdS nanorods, but with a $t^{-1/2}$ decay that corresponds to a universal, one-dimensional diffusion–annihilation reaction of electrons with surface-trapped holes.[16,17] The delayed emission is therefore likely determined by de-trapping rather than diffusion of holes at the surface. The lack of power law behaviour for the trap emission indicates a state with predictable recombination probability and is consistent with hole trapping at $Cd(OH)_2$ surface states close to the CdTe/CdS interface, followed by radiative recombination with a strongly confined electron that is localised in close proximity.

After $CdCl_2$ treatment of the tipped rods the lifetime of the TA signal for B4 increased from τ_1 = 2 ps and τ_2 = 73 ps to a

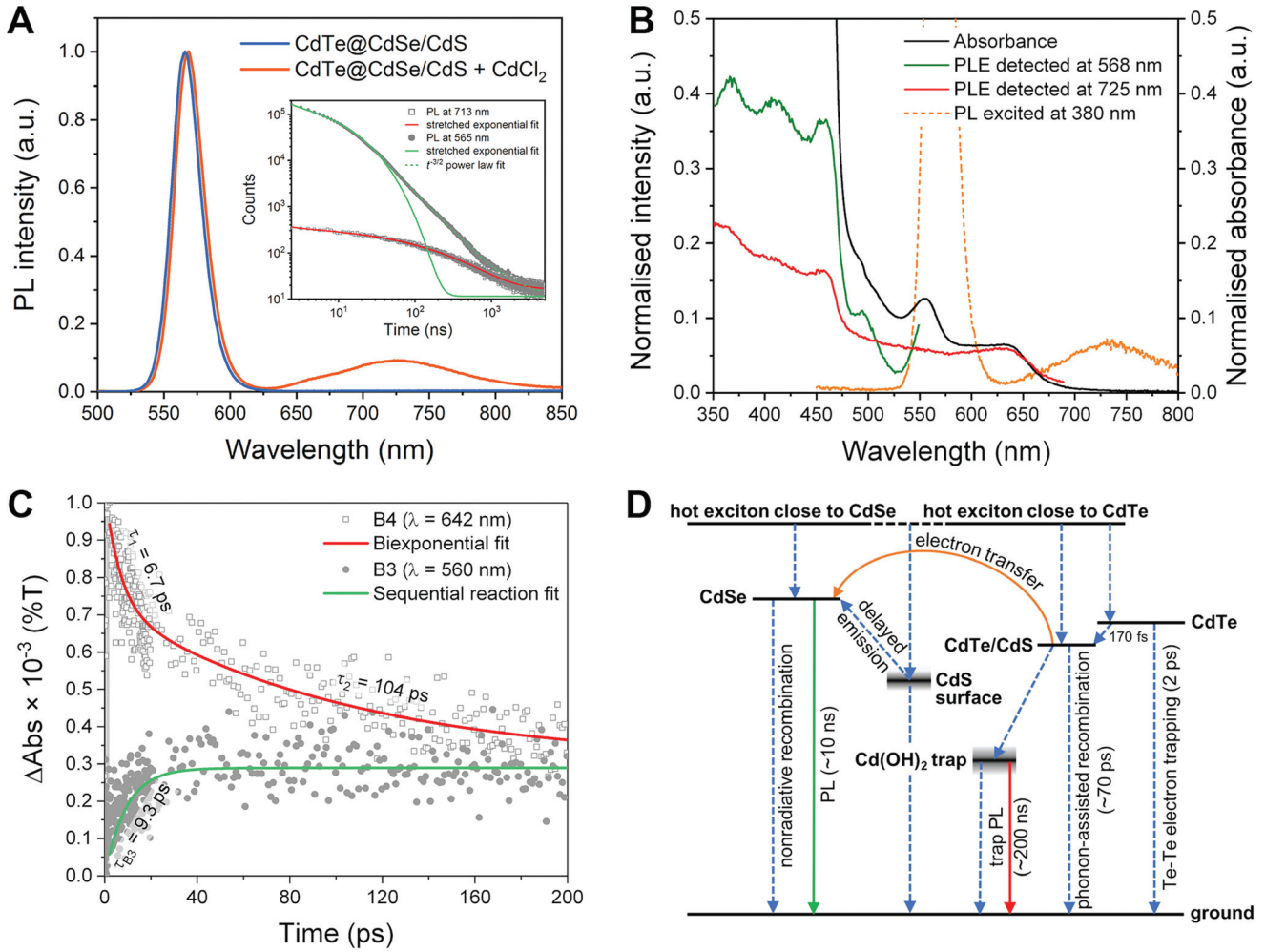

Fig. 6 (A) Normalised PL spectra of CdTe@CdSe/CdS (2.9 nm seed) before (blue) and after (orange) treatment with $CdCl_2$. The inset shows the decay for PL at 713 nm (red) and 565 nm (green). The latter exhibits a tail that appears linear in the log–log plot and was fit with a power law. (B) PL excitation spectra of the $CdCl_2$-treated, tipped nanorods acquired at the PL maxima of the emission from CdSe (green) and CdTe/CdS (red). Also shown are the absorption spectrum in black and the PL spectrum in orange. (C) Time traces of B4 (red) and B3 (green) after $CdCl_2$ treatment, pumped at 640 nm. The data have been fit to a biexponential decay (B4) and sequential reaction kinetics (B3), respectively. (D) Qualitative Jablonski diagram that summarises the possible transitions in CdTe@CdSe/CdS discussed in the text.

single exponential with τ = 480 ps. A weak signal for B3 grew in with a time constant τ_{B3} = 9.3 ps and did not decay within the timeframe of the experiment (200 ps, see Fig. 6B and ESI, Fig. S21–S23†). Signal transfer from B4 to B3 increased from 11 to 40%, compared to untreated CdTe@CdSe/CdS. It is therefore possible to switch off the detrimental, fast relaxation that competes with electron delocalisation. The observed decay of B4 after surface passivation is faster than that of pure CdTe. We attribute this to interfacial defects that are not affected by the treatment. This effect can in principle be countered by introduction of a graded interface to mitigate point defects.[1,2,66] However, a fast, non-radiative channel is required to define the off state when using the model system for switching. Interestingly, the surface treatment also suppressed hole-extraction by 4-MPH. This effect is not surprising, because of a tendency of the treated particles to aggregate and thus blocking diffusion of the hole scavenger to the particle surface. Furthermore, $CdCl_2$ is expected to change the surface polarity and drastically reduce access and available binding sites for electron pair donor (L-type) ligands such as 4-MPH. The possible transitions in our model have been summarised in the diagram if Fig. 6D.

Conclusion

The experiments presented here demonstrate the possibility to switch a photoactive nanostructure between a defined on and off state. The switching is based on the synergy of lattice mismatch, trap states, and coulomb attraction, which are usually regarded as detrimental effects. We have shown at the example of CdTe@CdSe/CdS nanorods with an axial heterointerface that exciton dissociation in strained type-II structures is suppressed by a combination of strain-induced band bending, size quantisation of the potential barrier, and coulomb attraction of the charge carriers. The off state is defined by fast, non-radiative dissipation of the excitation energy *via* electron–phonon coupling mediated by the strong spatial confinement of the charge carriers at opposite sides of the heterointerface. The long-lived on state is created by providing a hole acceptor that extracts the hole on a timescale that is competitive with the trapping. This process removes the coulomb contribution to the potential well of the electron, which then relocates into the region of lowest energy, provided by a CdSe reporter particle in our model system. Relaxation channels based on surface traps that reduce the overall quantum yield of the system but are unrelated to the mechanism discussed here can be closed by surface passivation. For applications the reporter particle may be left out or replaced by a metal particle on the surface as electronic contact or to drive photocatalytic reaction.

Author contributions

F.E. developed and carried out the synthesis and characterisation of the nanoparticles, contributed to the evaluation of results from transient absorption experiments and performed effective mass approximation calculations. K.B. conceived the experiments and contributed to the calculations and evaluation of the data. A.B., J.L., and P.Z. performed transient absorption experiments, under supervision of D.B. and T.A.S. The manuscript was written by F.E. and K.B. with contributions from all authors. All authors have given approval to the final version of the manuscript.

Conflicts of interest

There are no conflicts to declare.

Acknowledgements

This work was supported by the DFG project BO4516/3-1 and the DAAD-UAus project "Mapping ultrafast energy relaxation in semiconductor nanocrystals". K. B. is grateful for financial support by the Fonds der Chemischen Industrie *via* a Liebig Fellowship and the Zukunftskolleg Konstanz *via* a 5-year Marie Curie ZIF Research Fellowship. F. E. acknowledges financial support by the Fonds der Chemischen Industrie through a PhD scholarship. J. L. acknowledges funding by Toyota Motor Europe. D. B. acknowledges financial support from the Emmy Noether program (BR5030/1-1) of the German Research Foundation (DFG). T. A. S. and P. Z. acknowledge the support of the Australian Research Council Centre of Excellence in Exciton Science (CE170100026). The authors would like to thank Elena Sturm (née Rosseeva) for Cs-corrected TEM micrographs, as well as Stefanie Breimaier, Niklas Unglaube, Lisa Winkler, and Samuel Monter for work assisting the development of the tipped nanorod synthesis.

References

1 K. Boldt, N. Kirkwood, G. A. Beane and P. Mulvaney, *Chem. Mater.*, 2013, **25**, 4731–4738.
2 K. Boldt, K. N. Schwarz, N. Kirkwood, T. A. Smith and P. Mulvaney, *J. Phys. Chem. C*, 2014, **118**, 13276–13284.
3 K. Wu and T. Lian, *Chem. Soc. Rev.*, 2016, **45**, 3781–3810.
4 M. G. Lupo, F. Della Sala, L. Carbone, M. Zavelani-Rossi, A. Fiore, L. Lüer, D. Polli, R. Cingolani, L. Manna and G. Lanzani, *Nano Lett.*, 2008, **8**, 4582–4587.
5 D. Steiner, D. Dorfs, U. Banin, F. della Sala, L. Manna and O. Millo, *Nano Lett.*, 2008, **8**, 2954–2958.
6 A. Sitt, F. Della Sala, G. Menagen and U. Banin, *Nano Lett.*, 2009, **9**, 3470–3476.
7 Y. Luo and L.-W. Wang, *ACS Nano*, 2010, **4**, 91–98.
8 L. T. Kunneman, M. Zanella, L. Manna, L. D. A. Siebbeles and J. M. Schins, *J. Phys. Chem. C*, 2013, **117**, 3146–3151.
9 K. Wu, L. J. Hill, J. Chen, J. R. McBride, N. G. Pavlopolous, N. E. Richey, J. Pyun and T. Lian, *ACS Nano*, 2015, **9**, 4591–4599.

10 I. Angeloni, W. Raja, A. Polovitsyn, F. De Donato, R. P. Zaccaria and I. Moreels, *Nanoscale*, 2017, **9**, 4730–4738.
11 D. Dorfs, A. Salant, I. Popov and U. Banin, *Small*, 2008, **4**, 1319–1323.
12 N. N. Hewa-Kasakarage, M. Kirsanova, A. Nemchinov, N. Schmall, P. Z. El-Khoury, A. N. Tarnovsky and M. Zamkov, *J. Am. Chem. Soc.*, 2009, **131**, 1328–1334.
13 K. Wu, W. E. Rodríguez-Córdoba, Z. Liu, H. Zhu and T. Lian, *ACS Nano*, 2013, **7**, 7173–7185.
14 K. Wu, Y. Du, H. Tang, Z. Chen and T. Lian, *J. Am. Chem. Soc.*, 2015, **137**, 10224–10230.
15 S. Sánchez-Paradinas, D. Dorfs, S. Friebe, A. Freytag, A. Wolf and N. C. Bigall, *Adv. Mater.*, 2015, **27**, 6152–6156.
16 J. K. Utterback, A. N. Grennell, M. B. Wilker, O. M. Pearce, J. D. Eaves and G. Dukovic, *Nat. Chem.*, 2016, **8**, 1061–1066.
17 A. N. Grennell, J. K. Utterback, O. M. Pearce, M. B. Wilker and G. Dukovic, *Nano Lett.*, 2017, **17**, 3764–3774.
18 S. Itzhakov, H. Shen, S. Buhbut, H. Lin and D. Oron, *J. Phys. Chem. C*, 2013, **117**, 22203–22210.
19 Y. Dong, R. Wu, P. Jiang, G. Wang, Y. Chen, X. Wu and C. Zhang, *ACS Sustainable Chem. Eng.*, 2015, **3**, 2429–2434.
20 Z. Deutsch, O. Schwartz, R. Tenne, R. Popovitz-Biro and D. Oron, *Nano Lett.*, 2012, **12**, 2948–2952.
21 Z. Deutsch, L. Neeman and D. Oron, *Nat. Nanotechnol.*, 2013, **8**, 649–653.
22 S. Kudera, L. Carbone, M. F. Casula, R. Cingolani, A. Falqui, E. Snoeck, W. J. Parak and L. Manna, *Nano Lett.*, 2005, **5**, 445–449.
23 K. P. Acharya, R. S. Khnayzer, T. O'Connor, G. Diederich, M. Kirsanova, A. Klinkova, D. Roth, E. Kinder, M. Imboden and M. Zamkov, *Nano Lett.*, 2011, **11**, 2919–2926.
24 T. Mokari, E. Rothenberg, I. Popov, R. Costi and U. Banin, *Science*, 2004, **304**, 1787–1790.
25 S. E. Habas, P. Yang and T. Mokari, *J. Am. Chem. Soc.*, 2008, **130**, 3294–3295.
26 J. Maynadié, A. Salant, A. Falqui, M. Respaud, E. Shaviv, U. Banin, K. Soulantica and B. Chaudret, *Angew. Chem., Int. Ed.*, 2009, **48**, 1814–1817.
27 L. Carbone, A. Jakab, Y. Khalavka and C. Sönnichsen, *Nano Lett.*, 2009, **9**, 3710–3714.
28 A. M. Smith, A. M. Mohs and S. Nie, *Nat. Nanotechnol.*, 2008, **4**, 56–63.
29 S. Christodoulou, F. Rajadell, A. Casu, G. Vaccaro, J. Q. Grim, A. Genovese, L. Manna, J. I. Climente, F. Meinardi, G. Rainò, T. Stöferle, R. F. Mahrt, J. Planelles, S. Brovelli and I. Moreels, *Nat. Commun.*, 2015, **6**, 7905.
30 D. V. Talapin, I. Mekis, S. Götzinger, A. Kornowski, O. Benson and H. Weller, *J. Phys. Chem. B*, 2004, **108**, 18826–18831.
31 S. M. Fairclough, E. J. Tyrrell, D. M. Graham, P. J. B. Lunt, S. J. O. Hardman, A. Pietzsch, F. Hennies, J. Moghal, W. R. Flavell, A. A. R. Watt and J. M. Smith, *J. Phys. Chem. C*, 2012, **116**, 26898–26907.
32 O. Schöps, N. L. Thomas, U. Woggon and M. Artemyev, *J. Phys. Chem. B*, 2007, **110**, 2074–2079.
33 Y. Yan, G. Chen and P. G. Van Patten, *J. Phys. Chem. C*, 2011, **115**, 22717–22728.
34 L. Jing, S. V. Kershaw, T. Kipp, S. Kalytchuk, K. Ding, J. Zeng, M. Jiao, X. Sun, A. Mews, A. L. Rogach and M. Gao, *J. Am. Chem. Soc.*, 2015, **137**, 2073–2084.
35 S. G. Kumar and K. S. R. K. Rao, *Energy Environ. Sci.*, 2014, **7**, 45–102.
36 T. D. Lee and A. U. Ebong, *Renewable Sustainable Energy Rev.*, 2017, **70**, 1286–1297.
37 Q. Zeng, X. Kong, Y. Sun, Y. Zhang, L. Tu, J. Zhao and H. Zhang, *J. Phys. Chem. C*, 2008, **112**, 8587–8593.
38 D. Dorfs, T. Franzl, R. Osovsky, M. Brumer, E. Lifshitz, T. A. Klar and A. Eychmüller, *Small*, 2008, **4**, 1148–1152.
39 Y. Nonoguchi, T. Nakashima and T. Kawai, *Small*, 2009, **5**, 2403–2406.
40 T. Watanabe, K. Takahashi, K. Shimura and D. Kim, *Phys. Rev. B*, 2017, **96**, 035305.
41 S. Rawalekar, S. Kaniyankandy, S. Verma and H. N. Ghosh, *J. Phys. Chem. C*, 2010, **114**, 1460–1466.
42 L. Carbone, C. Nobile, M. de Giorgi, F. D. Sala, G. Morello, P. Pompa, M. Hytch, E. Snoeck, A. Fiore, I. R. Franchini, M. Nadasan, A. F. Silvestre, L. Chiodo, S. Kudera, R. Cingolani, R. Krahne and L. Manna, *Nano Lett.*, 2007, **7**, 2942–2950.
43 J. Lauth, G. Grimaldi, S. Kinge, A. J. Houtepen, L. D. A. Siebbeles and M. Scheele, *Angew. Chem., Int. Ed.*, 2017, **56**, 14061–14065.
44 A. Grupp, A. Budweg, M. P. Fischer, J. Allerbeck, G. Soavi, A. Leitenstorfer and D. Brida, *J. Opt.*, 2018, **20**, 014005.
45 B. Sadtler, D. O. Demchenko, H. Zheng, S. M. Hughes, M. G. Merkle, U. Dahmen, L.-W. Wang and A. P. Alivisatos, *J. Am. Chem. Soc.*, 2009, **131**, 5285–5293.
46 G. Bertoni, V. Grillo, R. Brescia, X. Ke, S. Bals, A. Catellani, H. Li and L. Manna, *ACS Nano*, 2012, **6**, 6453–6461.
47 Y. He, H.-T. Lu, L.-M. Sai, W.-Y. Lai, Q.-L. Fan, L.-H. Wang and W. Huang, *J. Phys. Chem. B*, 2006, **110**, 13370–13374.
48 A. Trellakis, T. Zibold, T. Andlauer, S. Birner, R. K. Smith, R. Morschl and P. Vogl, *J. Comput. Electron.*, 2006, **5**, 285–289.
49 S. Adachi, *Properties of Group-IV, III-V and II-VI Semiconductors*, John Wiley & Sons, Ltd, Chichester, 1st edn, 2005.
50 S.-H. Wei and A. Zunger, *Appl. Phys. Lett.*, 1998, **72**, 2011.
51 A. Zunger, *Phys. Status Solidi B*, 2001, **224**, 727–734.
52 K. Wu, H. Zhu and T. Lian, *Acc. Chem. Res.*, 2015, **48**, 851–859.
53 J. J. Snellenburg, S. P. Laptenok, R. Seger, K. M. Mullen and I. H. M. van Stokkum, *J. Stat. Softw.*, 2012, **49**, 1–22.
54 R. R. Cooney, S. L. Sewall, E. A. Dias, D. M. Sagar, K. E. H. Anderson and P. Kambhampati, *Phys. Rev. B: Condens. Matter Mater. Phys.*, 2007, **75**, 245311.
55 A. Franceschetti, H. Fu, L. W. Wang and A. Zunger, *Phys. Rev. B: Condens. Matter Mater. Phys.*, 1999, **60**, 1819–1829.
56 C. Mauser, E. Da Como, J. Baldauf, A. L. Rogach, J. Huang, D. V. Talapin and J. Feldmann, *Phys. Rev. B: Condens. Matter Mater. Phys.*, 2010, **82**, 081306.

57 S. F. Wuister, C. de Mello Donegá and A. Meijerink, *J. Phys. Chem. B*, 2004, **108**, 17393–17397.
58 G. A. Beane, K. Boldt, N. Kirkwood and P. Mulvaney, *J. Phys. Chem. C*, 2014, **118**, 18079–18086.
59 R. A. Street, *Solid State Commun.*, 1977, **24**, 363–356.
60 S. C. Boehme, J. M. Azpiroz, Y. V. Aulin, F. C. Grozema, D. Vanmaekelbergh, L. D. A. Siebbeles, I. Infante and A. J. Houtepen, *Nano Lett.*, 2015, **15**, 3056–3066.
61 P. Zeng, N. Kirkwood, P. Mulvaney, K. Boldt and T. Smith, *Nanoscale*, 2016, **8**, 10380–10387.
62 G. A. Beane, K. Gong and D. F. Kelley, *ACS Nano*, 2016, **10**, 3755–3765.
63 N. Kirkwood, J. O. V. Monchen, R. W. Crisp, G. Grimaldi, H. A. C. Bergstein, I. du Fossé, W. van der Stam, I. Infante and A. J. Houtepen, *J. Am. Chem. Soc.*, 2018, **140**(46), 15712–15723.
64 M. Kuno, D. Fromm, H. Hamann, A. Gallagher and D. Nesbitt, *J. Chem. Phys.*, 2000, **112**, 3117–3120.
65 F. T. Rabouw, M. Kamp, R. J. A. van Dijk Moes, D. R. Gamelin, A. F. Koenderink, A. Meijerink and D. Vanmaekelbergh, *Nano Lett.*, 2015, **15**, 7718–7725.
66 K. Boldt, C. Ramanan, A. Chanaewa, M. Werheid and A. Eychmüller, *J. Phys. Chem. Lett.*, 2015, **6**, 2590–2597.